A simple approach for characterizing the spatially varying sensitivity of microchannel plate detectors

Cite as: Rev. Sci. Instrum. **93**, 075108 (2022); https://doi.org/10.1063/5.0092346 Submitted: 22 March 2022 • Accepted: 08 June 2022 • Published Online: 11 July 2022

Denis Aglagul, Denis Aglagul, Brian Kaufman, Chuan Cheng, et al.







ARTICLES YOU MAY BE INTERESTED IN

3D velocity map imaging of electrons with TPX3CAM

Review of Scientific Instruments 93, 013003 (2022); https://doi.org/10.1063/5.0071804

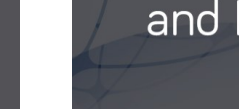
The ultrafast pixel array camera system and its applications in high energy density physics Review of Scientific Instruments 93, 074702 (2022); https://doi.org/10.1063/5.0091824

Imaging-based feedback cooling of a levitated nanoparticle

Review of Scientific Instruments 93, 075109 (2022); https://doi.org/10.1063/5.0095614

Review of Scientific Instruments

Read Now!



Special Issue: Advances in Measurements and Instrumentation Leveraging Embedded Systems



A simple approach for characterizing the spatially varying sensitivity of microchannel plate detectors

Cite as: Rev. Sci. Instrum. 93, 075108 (2022); doi: 10.1063/5.0092346

Submitted: 22 March 2022 • Accepted: 8 June 2022 •

Published Online: 11 July 2022







Denis Aglagul, Denis Aglagul, Denis Aglagul, Denis Aglagul, Denis Aglagul, Denis Aglagul, Denis Saule, Denis Aglagul, Denis Ag

AFFILIATIONS

- ¹ Department of Physics and Astronomy, Stony Brook University, Stony Brook, New York 11794-3800, USA
- Department of Physics, University of Connecticut, Storrs, Connecticut 06269-3046, USA
- ³ Physics Department, Brookhaven National Laboratory, Upton, New York 11973, USA
- a) Author to whom correspondence should be addressed: thomas.weinacht@stonybrook.edu

ABSTRACT

We present a simple approach to characterize the spatial variation of the gain in microchannel plate (MCP) coupled to phosphor detectors using single electron or photon hits. The technique is easy to implement and general enough to be extended to other kinds of detectors. We demonstrate the efficacy of the approach on both laboratory and Monte Carlo generated datasets. Furthermore, we use the approach to measure the variation in gain over time as the MCP is exposed to an increasing number of electrons.

Published under an exclusive license by AIP Publishing. https://doi.org/10.1063/5.0092346

I. INTRODUCTION

Spatially resolved detection of electrons, ions, and photons plays an important role in many areas of physics, chemistry, biology, and astronomy. 1-7 Intrinsic to all spatially resolved detectors is a spatial variation in the response.^{8,9} This spatial variation can be exacerbated as the detector is exposed to a spatially non-uniform signal over time. Microchannel plates (MCPs), which are typically used to amplify single electrons, ions, or photons, while maintaining spatial resolution, become depleted in regions of high ion/electron exposure. 10-12 For multilayer MCPs, the last MCP in the series will experience the worst gain depreciation as it has to handle several orders of magnitude of more charges passing through it. 12 For MCP based imaging and spectroscopy systems, such as the Chandra High-Resolution Camera (HRC), temporal and spatial uniformity of gain is necessary for successful operation.4 Characterizing the spatial variation in the gain (detector response) can be challenging because it is difficult to disentangle the spatial variation in the signal from the spatial variation in the detector response. In the worst case sce-nario, the gain in a given region could become so low that it becomes a "dead spot" on the detector. The traditional approach to char-acterizing a detector's response relies on exposing the detector to

a known distribution of electrons or photons—ideally a uniform spatial distribution of electrons ("flat-fielding"). 9.11,13-18 A fast pulsed, uniform distribution of energetic radiation is technically challenging to produce and difficult to characterize. The aforementioned Chandra HRC needs annual gain calibration for in flight measurements. Unable to produce flat-fields in orbit due to celestial x-ray sources having complex spectra and temporal variability, the team relies on a high resolution flat-fielded gain correction map as a basis, which is modified for each epoch by a correction factor computed by comparing observed and expected count rates at 21 observation locations. 19 In order to develop the initial gain map for the Chandra HRC, the instrument was transported to the Smithsonian Astrophysical Observatory where a facility was tailor made so each segment of the HRC could be uniformly illuminated. 20

Here, we present an alternative approach that makes use of the fact that all single charged particles incident on the detector carry the same charge regardless of their source or distribution. This technique takes advantage of centroided single electron/ion/photon hits²¹ from any source. The only necessary condition is hit identification, which requires that hits must be infrequent or dispersed enough such that overlapping hits are uncommon.

II. NEW APPROACH

Our approach follows the following steps (for the single pixel approach discussed below):

- We initialize two arrays corresponding to the pixel sensor array on the camera: a sum array (sum over grayscale values for the brightest pixels within hits) and a count array (the number of times a pixel was within a hit).
- We identify individual hits on the detector by identifying contiguous pixels that surpass a predetermined threshold value.
- 3. Within each hit, we identify the pixel that has the highest intensity (brightest pixel).
- 4. (Optional) The brightest pixel value can be assigned to all pixels in a rectangle encompassing the hit in order to increase the speed of the characterization (bounding box approach).
- 5. We calculate a sum of brightest pixel values (sum array) and the number of times each pixel was identified as the brightest pixel (count array).
- 6. We divide the sum array by the count array to arrive at a raw sensitivity map.
- We normalize the sensitivity map by the largest element (or 99th quantile) for the final result.

As each electron or ion that is incident on the front of the detector has the same charge and, thus, should ideally generate exactly the same total charge at the back of the MCPs and the same amount of light from the phosphor, a measurement of the actual intensity for each hit can be used to map the gain or sensitivity at each point. Averaging the intensities measured for a large number of hits can compensate for the natural statistical fluctuations in gain (which lead to a finite width of the pulse height distribution) for any given point on the detector and, thus, produce a map of the position dependent detector response.

Our approach utilizes a simple centroiding algorithm to locate each hit on the detector and extract its center, intensity, and

bounding-box [smallest rectangle enclosing a single hit—bounding-box (BB)]. The left panel of Fig. 1 shows one image with several well separated hits of varying intensity and size. We extract the brightest pixel-value and extend it to the entire hit—i.e., the region enclosed by the BB. We repeat this for each hit in the image (middle panel) and then for each image in the measurement until the detector has been thoroughly populated with hits. The right most panel of Fig. 1 is a partially developed sensitivity map where the colorbar shows the normalized response (NR).

III. SIMULATION

In order to test our approach, we simulated the reconstruction of a detector sensitivity map using a Monte Carlo simulation. We make the following assumptions:

- 1. All photons and electrons are identical, so any variation in signal intensity is strictly due to our detector.
- The response function of the detector changes slowly across the span of a single hit, and we can describe the signal we record on the camera, S, at each pixel location (i, j) as the product of the detector's response function, R, and the distribution for each hit, H,

$$S(i,j) = R(i,j) \times H(i,j). \tag{1}$$

As shown in the top left panel of Fig. 2, we created a sensitivity map in the form of the letters SBU with varying sensitivity throughout the letters. The MCP point spread function has been modeled as a Gaussian, Lorentzian, and double Gaussian. For simplicity, we model the electron cloud footprint as a Gaussian of size (σ_i and σ_j),

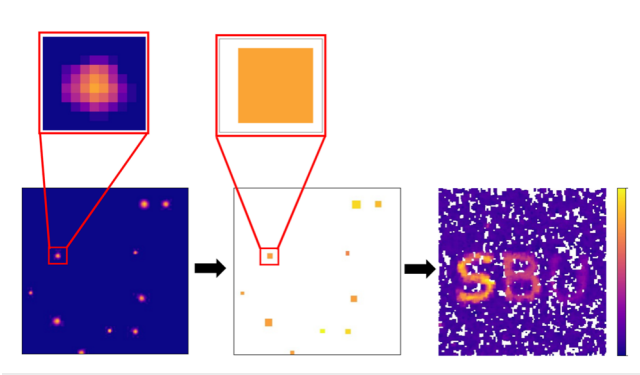


FIG. 1. Illustration of our approach to characterizing the spatial variation of the detector response. The left large panel shows a single frame from the camera with several hits (single electrons) on the detector. The middle large panel shows how we assign a uniform response for the pixels over threshold within each hit, and the right large panel illustrates the recovered detector response for a test case with around 5000 hits. The top small inset panels show a single hit and the uniform response value we assign to the pixels within each hit (within the "bounding-box").

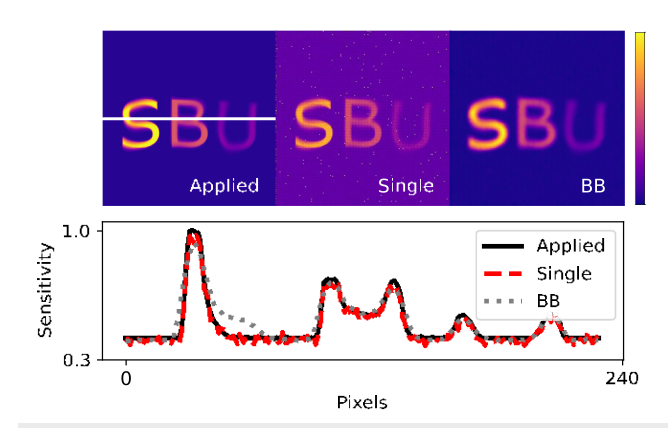


FIG. 2. Monte Carlo results showcasing the efficacy of our algorithm. The top left panel shows the applied detector response, the middle panel shows the recovered response using single pixels, and the top right panel shows the response recovered using the highest pixel response over the entire bounding-box for a given hit. The white line in the leftmost image is where we took a lineout from each map, which is shown plotted together in the bottom figure. The red dashed line is the result of treating a hit as a single pixel and the gray dotted line is extending the extracted gray-level to the bounding-box (BB) of the hit.

and height A, (average value with a normal distribution) at different locations on the grid (i, j) with the center at (i_0, j_0) ,

$$H(i,j) = A \exp \left(\Box \frac{(i \Box i_0)^2}{\sigma_i^2} \Box \frac{(j \Box j_0)^2}{\sigma_i^2} \right)$$
 (2)

Each hit is multiplied by the detector's response function, which we describe by $R(i,j) = \theta_{i_0j_0} + \alpha_{ij}[(i \Box i_0) + (j \Box j_0)]$, where $\theta_{i_jj_0}$ describes the response at each pixel and α_{ij} describes the spatial variation of the response (i.e., derivative of the response function). A slow variation of the response function with position corresponds to α_{ij} being small compared to $\theta_{i_0j_0}$ (assumption 2). This is particularly relevant for the bounding box approach described below to be successful.

The amplitude A serves as our measure of intensity, where the single brightest pixel within a hit's bounding-box serves as the height and center of that event. The signal centered at pixel $(i=i_0,j=j_0)$ can be expressed as

$$S(i_0, j_0) = R(i_0, j_0) \times H(i_0, j_0) = \theta_{i_0 j_0} A.$$
 (3)

We calculate the average signal, $\theta_{i,j_0}A$, for every pixel in order to create a sensitivity map. From assumption 1 above, we know the intensity of each hit, A, has the same expected value everywhere, so the pixel to pixel variation on our map is primarily due to the channel to channel gain variation on the detector. The NR of the detector for an imaging pixel (i₀, j₀) is simply

$$\frac{\theta_{i_0 j_0} A}{\theta_{\text{max}} A} = \theta_{i_0 j_0} / \theta_{\text{max}}, \tag{4}$$

where $\boldsymbol{\theta}_{\text{max}}$ is the largest recorded detector response. Thus, the relative response of the combined MCP-phosphor detector imaged with pixel (i_0, j_0) is simply $\theta_{i,i}/\beta_{max}$. Figure 2 shows a comparison of the detector NR analysis when using a single brightest pixel (SBP) approach (top row, middle panel) vs a bounding-box (BB) approach (top row, right panel). From the top row of the figure, it can be seen that both the SBP and BB analyses qualitatively capture the NR of the sensor. More quantitatively, the bottom panel of Fig. 2 shows a lineout analysis of the two methods. The bottom panel shows lineouts of the NR for the original image, the recovered NR based on Monte-Carlo generated data using the single-pixel approach, and the recovered NR based on Monte-Carlo generated data using the BB approach. The only disagreement between the three curves is in the region of the applied mask where the NR varies rapidly with position, violating one of the approximations required for the BB approach to work.

Given the fact that any point on the detector has a finite pulse height distribution, one needs to have more than one hit per pixel for the sensitivity map to be a reliable estimator of the detector. Figure 3 shows the root mean square (rms) difference between the recovered and applied sensitivity maps as a function of the average number of hits on a given pixel. We ran Monte Carlo simulations for various numbers of hits and calculated the average hits per pixel to quantify the accuracy of the method. We note that the rms difference calculation only takes into account pixels that received hits. Figure 3 shows that increasing the average number of hits per pixel greatly improves the accuracy, which suggests that our sensitivity map is an

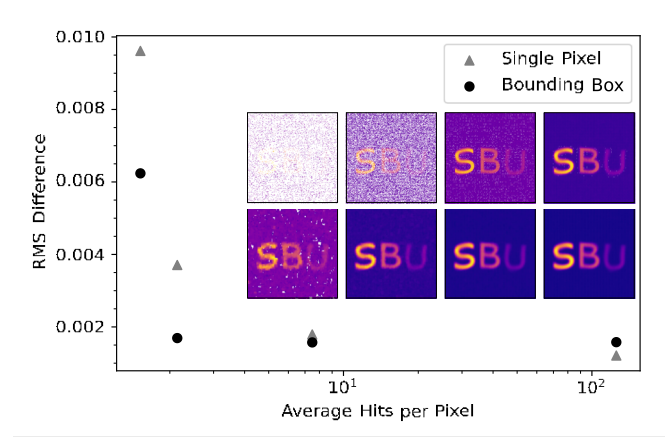


FIG. 3. The rms difference between the recovered and programmed sensitivity maps for different numbers of hits per illuminated pixel (pixels not illuminated are excluded from the calculation) on a 240×240 grid. These are the same simulations as Fig. 2. For 5k, 50k, 500k, and 5000k hits, the sensitivity maps produced are presented as an inset on the top right with the top row showing the single pixel values and the bottom row showing the bounding-box values.

asymptotically unbiased estimator. At 10 hits per pixel, the sensitivity map begins to converge to the true response function of the detector resulting in a faithful reconstruction of our programmed sensitivity map.

Collecting enough data to satisfy 10 hits per pixel might be difficult, depending on the source of the hits. If the response on the detector does not change quickly within the span of a hit (i.e., α_{ij} is small, assumption 2), neighboring pixels (those within the bounding-box of the Gaussian) can be assigned the same value as the central pixel, A, leading to the same signal as described by Eq. (4) for all pixels in the hit, thus a more rapid characterization of the detector response. The top right panel of Fig. 2 shows the recov-ered sensitivity map using this method. The bottom panel of Fig. 2 shows a lineout in the gray dotted line of this bounding-box value compared to the single pixel value and the applied sensitivity map. The bounding-box value compares well except in the pixel region around the "S." In this region, the response changes too quickly for the algorithm, thus assumption 2 becomes invalid. The boundingbox value needs a slowly changing response in the span of a hit to accurately measure the sensitivity at the point. When this condition is met, which is often the case, the bounding-box and single pixel values both compare well. Furthermore, we can see from Fig. 3 that the bounding-box value reaches the same accuracy as the single pixel value for an average of 10 hits per pixel at only 3 hits per pixel, which requires many fewer hits.

IV. EXPERIMENT

The beauty of this new characterizing approach is its simplicity: the only requirements are a source of hits and a camera to record those hits on the detector. Each particle causes a cascade of electrons from the first MCP, which are further amplified by the second MCP. The resulting cloud of electrons is accelerated a short distance where they hit a phosphor screen producing photons on the opposite side. These photons are imaged by a camera and analyzed using the approach described above to generate a sensitivity map

of the combined MCP-phosphor detector. The source of hits and their distribution does not matter as long as the hits cover the region of the detector that one is interested in mapping. We demonstrate the characterization of detector responses generated using extreme ultraviolet (XUV) photons and electrons for several different detectors and using both traditional frame driven cameras and event driven cameras.

We performed measurements on a dual stack rectangular shaped MCP and phosphor screen, used inside an XUV spectrometer. The detector was located at the Fourier plane of the XUV spectrometer and could be illuminated by a combination of XUV photons generated via high harmonic generation²⁵ and dispersed by the XUV spectrometer (producing a series of vertical stripes), or electrons from an ionization gauge located in the same vacuum chamber. The light from the phosphor screen was measured with a frame driven camera (ORCA-Flash 4.0, digital CMOS Camera, C11440-22CU). Comparing sensitivity maps with both types of sources highlights the fact that the source of the hits does not matter for recovering a sensitivity map of the detector.

Another series of measurements were performed on a circular dual stack MCP detector with a P46/P47 phosphor screen, which is part of a velocity map imaging apparatus. The vacuum chamber is equipped with a residual gas analyzer, which produced a steady stream of electrons across the entire detector. We characterized this detector under three different conditions: (1) using an old worn set of MCPs and P46 phosphor screen both with significant depletion, (2) a brand new set of MCPs with P47 phosphor screen, and (3) the same new set following an incident that caused arcing damage between the back MCP and phosphor screen.

First, we performed a comparison between the old and new detectors, (1) and (2), using a frame driven camera. We used a Basler acA640-750um CMOS camera outfitted with a Fujinon 12.5 mm f/1.4 lens to measure the old detector and a Navitar 17 mm f/0.95 lens to measure the new detector. The Basler camera acquires images at rates up to 1 kHz, 21 with integration times between 59 μ s and several milliseconds. It provides a grayscale value (e.g., a value from 0 to 255 for an 8-bit camera) for each pixel integrated over some

predetermined acquisition time. By comparing sensitivity maps of these drastically different detectors, we can demonstrate how well this approach captures the changes in sensitivity of the detectors over time.

Second, we performed a comparison of the new but damaged detector (3) using two different cameras. One was the frame driven Basler with the Navitar lens and the other was an event driven camera with ns-scale timing resolution, called the TPX3CAM, ^{26,27} equipped with a Navitar 50 mm f/0.95 lens. The camera provides a time of arrival and time over threshold (ToT) for each pixel over the array when the signal in the pixel exceeds a predefined threshold. The ToT values are proportional to the charge detected by pixels and are digitized with 10 bit precision. Comparing sensitivity maps taken with the two different kinds of cameras demonstrates that the time over threshold can be used as a rough proxy for grayscale values.

V. EXPERIMENTAL RESULTS

We started by characterizing the rectangular MCPs in the XUV spectrometer shown in Fig. 4. This figure highlights the effectiveness of our approach for very different distributions of incident particles. The top left panel shows the normalized yield (normalized sum of all hits) when exposing the detector to electrons from an ionization gauge, while the bottom left panel shows the normalized yield when exposing the detector to a combination of these same electrons from the ionization gauge and the XUV photons from the XUV spectrometer. The right panels show the recovered detector response for the two different sources. Note that while the left panels are very different as a result of the XUV photons from the spectrometer having a very different distribution than the electrons from the ionization gauge, the right two panels are almost identical, highlighting the ability of the algorithm to recover the detector response regardless of how the incident particles are distributed. It is known that the particle velocity and species influence MCP secondary electron yields, as well as hit size, which is correlated with the gain of the MCP.²⁸ Our algorithm has demonstrated an indifference to whether photons or electrons are used as a source and the same may be true for ion

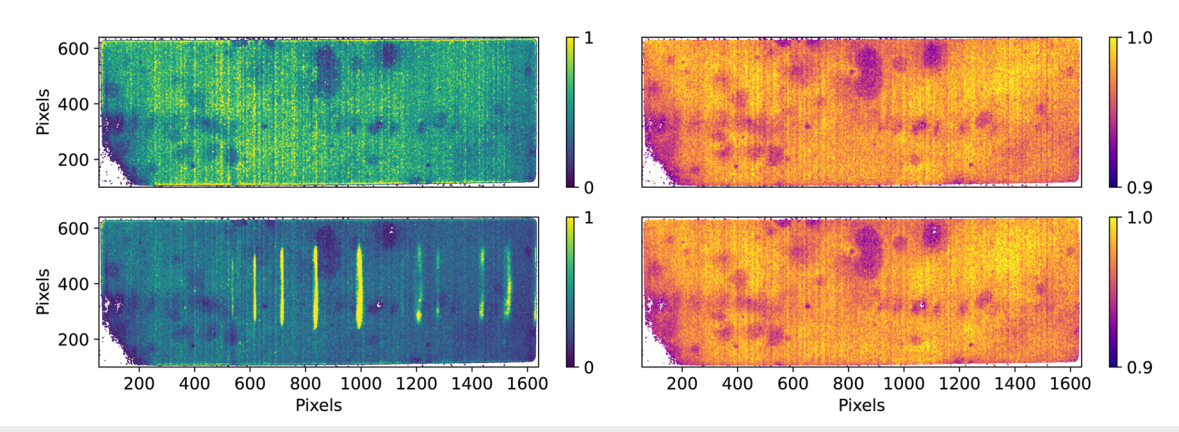


FIG. 4. Sensitivity maps of a rectangular dual-stack MCP-phosphor detector (right column) using two different sources of hits with different distributions (left column). The source for the top row is electrons from an ionization gauge, whereas the bottom row has XUV photons from HHG in addition to the electrons from the ionization gauge. The detector is imaged with a C11440-22CU ORCA-Flash 4.0, digital CMOS Camera. All sensitivity maps are normalized by the 99th quantile rather than the maximum value to avoid statistical fluctuations.

species, although further work is needed to confirm this. In order to make the comparison, we collected the same number of hits for each map, working in a regime of equal hits from electrons and XUV photons.

Next, we considered the characterization of two detectors in a velocity map imaging apparatus^{2,12}—an old one that has been used for many years (1) and a new detector (2), as described previously. These results are presented in Fig. 5, which shows the measured detector responses as well as the pulse height distributions (PHD). The black vertical line in the pulse height distribution histograms indicates where we chose the grayscale value threshold for detecting hits. This value was chosen to minimize contamination from noisy pixels while still capturing the majority of all hits. Our old detector has been bombarded with enough hits near the center such that the gain is severely depleted, and the light produced from the center of the phosphor screen does not go above the noise floor of the camera. This leads to the dead spot in the center, which cannot be solved by lowering the threshold since this would simply lead to noise from the camera being mistaken for hits on the detector.

In addition to demonstrating the approach for different sources of hits, we demonstrate the approach for different cameras. Figure 6 shows the comparison of the sensitivity maps for an event driven camera (TPX3CAM)^{30,31} and a frame driven camera (Basler) for the new but damaged detector (3). Overall, the sensitivity maps generated by both cameras are quite similar. The damage spots on the detector due to the arcing, which appear as purple blobs on the edge of the map, particularly at 1, 5, 6, and 9 o'clock, present an excellent feature for comparison. The algorithm is able to recover the damage spots using both camera methods illustrating that a sensitivity map generated from the time over threshold (ToT) of the event driven camera is roughly equivalent to the sensitivity map generated from the grayscale values of the frame driven camera.

This new method is not only able to measure large scale depletion as described in Fig. 5 but also lesser damage due to arcing. The detector shown in Fig. 6 is actually the same as the new detector shown in Fig. 5; however, Fig. 6 is shown following an incident that caused arcing between the back MCP and phosphor screen. We were able to confirm by direct observation of the MCPs and phosphor screen that the location of the damage spots (purple blobs

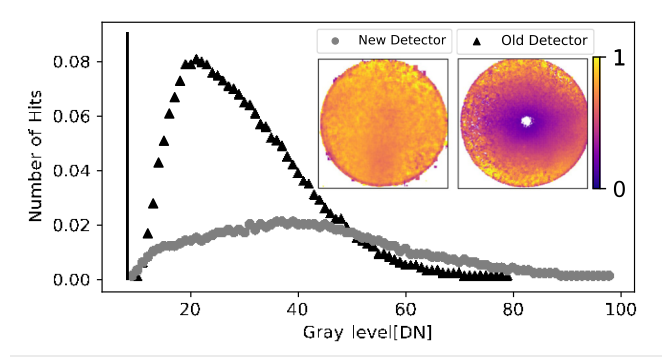


FIG. 5. Detector response functions (inset) and pulse height distributions for old and new MCP + phosphor detectors, (1) and (2), in a velocity map imaging apparatus characterized with electrons from a residual gas analyzer. The vertical line indicates where the threshold value was established for using hits to characterize the detector.

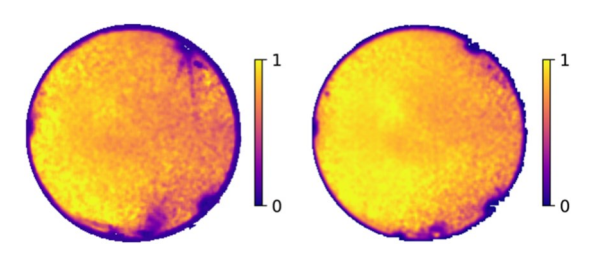


FIG. 6. Comparison of sensitivity maps generated from frame driven and event driven cameras for the new but damaged detector (3). The left is data taken with the TPX3CAM using Time over Threshold (ToT) as a measure of intensity and the right figure is our Basler camera with traditional grayscale values.

at 1, 5, 6, and 9 o'clock) in the sensitivity map corresponds to real damage on the detector.

VI. CHANGING SENSITIVITY WITH TIME

The response of any MCP will gradually degrade with continued use. However, there is also a rapid decrease in sensitivity for the first hundred or so events detected in a spot, which leads manufacturers to recommend a detector burn in Refs. 10, 12, and 32–34. After initial exposure, this decay levels off. We recently replaced our MCPs, so we had the unique opportunity to apply our technique to quantify how quickly the response of the MCPs changes and discovered that we could track detector burn in. In Fig. 7, we compare imaging pixels that captured the same number of hits to demonstrate how the response changes as a function of usage. For testing purposes, we only used RGA data that, for our apparatus, were biased toward one side of the detector. After 2 hours at 200 hits per second, our sensitivity map had a diminished spot that coincided with the RGA distribution.

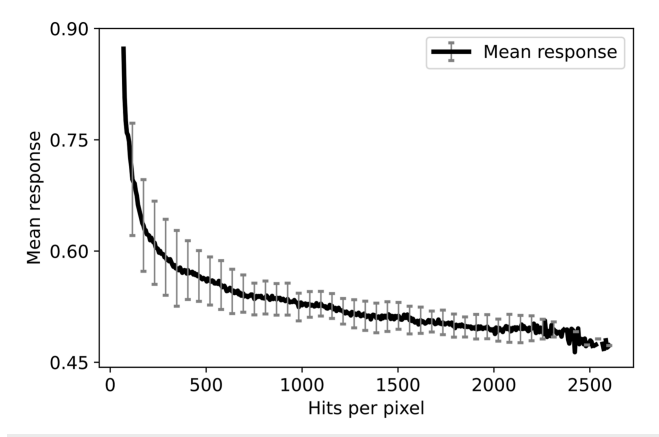


FIG. 7. Normalized response as a function of the total number of hits per pixel. The x axis describes the number of times a pixel has been illuminated, and the y axis is the average normalized response. Pixels that do not have enough statistics (less than 10 hits) are not included. The error bars are the standard deviation in response for pixels, which have detected an equal number of hits.

VII. CONCLUSION

In conclusion, we have demonstrated a simple and robust approach to characterizing the spatial variation in sensitivity of microchannel plate phosphor screen detectors. The approach makes use of single hits to characterize the position dependent detector response and works for charged particles as well as photons. The method works independent of the distribution of the incident particles and works for both frame driven and event driven cameras that image the phosphor screen.

ACKNOWLEDGMENTS

We gratefully acknowledge helpful discussions with Gönenç Moğol, Samuel McClung, and Eric Jones. This work was supported by the National Science Foundation (Award No. 2110376). T.S. was partially funded by the U.S. Department of Energy, Office of Science, Chemical Sciences, Geosciences, and Biosciences Division (Grant No. DE-SC0019098). The XUV spectrometer was developed under the Air Force Office of Scientific Research (Grant No. FA9550-17-1-0369).

AUTHOR DECLARATIONS

Conflict of Interest

The authors have no conflicts to disclose.

Author Contributions

Denis Aglagul: Conceptualization (lead); Data curation (lead); Formal analysis (lead); Investigation (lead); Methodology (lead); Software (equal); Validation (lead); Visualization (lead); Writing — original draft (lead); Writing — review & editing (equal). Brian Kaufman: Data curation (supporting); Investigation (supporting); Resources (equal); Supervision (equal); Writing — review & editing (equal). Chuan Cheng: Formal analysis (supporting); Investigation (supporting); Writing — review & editing (supporting). Thomas Weinacht: Funding acquisition (lead); Resources (lead); Supervision (equal); Writing — review & editing (equal). Tobias Saule: Data curation (supporting); Supervision (supporting); Writing — review & editing (supporting). Carlos A. Trallero-Herrero: Funding acquisition (equal); Investigation (supporting); Writing — review & editing (supporting). Andrei Nomerotski: Writing — review & editing (supporting).

DATA AVAILABILITY

The data collected for this manuscript is available upon request.

REFERENCES

- ¹R. Dörner, V. Mergel, O. Jagutzki, L. Spielberger, J. Ullrich, R. Moshammer, and H. Schmidt-Böcking, "Cold target recoil ion momentum spectroscopy: A 'momentum microscope' to view atomic collision dynamics," Phys. Rep. **330**, 95–192 (2000).
- ²A. T. J. B. Eppink and D. H. Parker, "Velocity map imaging of ions and electrons using electrostatic lenses: Application in photoelectron and photofragment ion imaging of molecular oxygen," Rev. Sci. Instrum. **68**, 3477–3484 (1997).

- ³C. L. Evans and X. S. Xie, "Coherent anti-Stokes Raman scattering microscopy: Chemical imaging for biology and medicine," Annu. Rev. Anal. Chem. **1**, 883–909 (2008).
- ⁴G. W. Fraser, "Imaging in astrophysics (and elsewhere)," Nucl. Instrum. Methods Phys. Res., Sect. A **471**, 170–173 (2001).
- ⁵C. D. Ertley, O. H. W. Siegmund, J. Hull, A. Tremsin, A. O'Mahony, C. A. Craven, and M. J. Minot, "Microchannel plate imaging detectors for high dynamic range applications," IEEE Trans. Nucl. Sci. **64**, 1774–1780 (2017).
- ⁶L. Conti, J. Barnstedt, L. Hanke, C. Kalkuhl, N. Kappelmann, T. Rauch, B. Stelzer, K. Werner, H.-R. Elsener, and D. M. Schaadt, "MCP detector development for UV space missions," Astrophys. Space Sci. **363**, 63 (2018).
- ⁷S. W. Hell, "Toward fluorescence nanoscopy," Nat. Biotechnol. **21**, 1347–1355 (2003).
- ⁸T. C. Williams and C. R. Shaddix, "Simultaneous correction of flat field and non-linearity response of intensified charge-coupled devices," Rev. Sci. Instrum. **78**, 123702 (2007).
- ⁹A. S. Tremsin, J. B. McPhate, J. V. Vallerga, O. H. W. Siegmund, J. S. Hull, W. B. Feller, and E. Lehmann, "High-resolution neutron radiography with microchannel plates: Proof-of-principle experiments at PSI," Nucl. Instrum. Methods Phys. Res., Sect. A **605**, 103–106 (2009).
- ¹⁰J. L. Wiza et al., "Microchannel plate detectors," Nucl. Instrum. Methods 162, 587–601 (1979).
- ¹¹C. D. Ertley, O. H. W. Siegmund, S. R. Jelinsky, J. Tedesco, M. J. Minot, A. O'Mahony, C. A. Craven, M. Popecki, A. V. Lyashenko, and M. R. Foley, "Second generation large area microchannel plate flat panel phototubes," Proc. SPIE 9915, 99152G (2016).
- ¹² A. Zhao, P. Sándor, and T. Weinacht, "Coincidence velocity map imaging using a single detector," J. Chem. Phys. **147**, 013922 (2017).
- ¹³ X. Wang, S. U. Setru, J. Xie, A. Mane, M. Demarteau, and R. Wagner, "Imaging of large-area microchannel plates using phosphor screens," J. Instrum. **9**, P11011 (2014).
- ¹⁴J. R. Kuhn, H. Lin, and D. Loranz, "Gain calibrating nonuniform image-array data using only the image data," Publ. Astron. Soc. Pac. **103**, 1097 (1991).
- ¹⁵ P. Boerner, C. Edwards, J. Lemen, A. Rausch, C. Schrijver, R. Shine, L. Shing, R. Stern, T. Tarbell, A. Title, C. J. Wolfson et al., "Initial calibration of the Atmospheric Imaging Assembly (AIA) on the Solar Dynamics Observatory (SDO)," in The Solar Dynamics Observatory (Springer, 2011), pp. 41–66.
- ¹⁶ N. Kardjilov, I. Manke, A. Hilger, M. Strobl, and J. Banhart, "Neutron imaging in materials science," Mater. Today **14**, 248–256 (2011).
- ¹⁷S. Koutchmy and A. Verlhac, "Photometric calibrations of an MCP space qualified photographic-camera," Astron. Astrophys. **142**, 355–360 (1985).
- ¹⁸ R. Hong, A. Leredde, Y. Bagdasarova, X. Fléchard, A. García, P. Müller, A. Knecht, E. Liénard, M. Kossin, M. G. Sternberg et al., "High accuracy posi-tion response calibration method for a micro-channel plate ion detector," Nucl. Instrum. Methods Phys. Res., Sect. A 835, 42–50 (2016).
- ¹⁹ A. T. Kenter, J. H. Chappell, R. P. Kraft, G. R. Meehan, S. S. Murray, M. V. Zombeck, K. T. Hole, M. Juda, R. H. Donnelly, D. Patnaude et al., "In-flight performance and calibration of the Chandra high-resolution camera imager (HRC-I)," Proc. SPIE **4012**, 467–492 (2000).
- ²⁰ A. T. Kenter, J. H. Chappell, K. Kobayashi, R. P. Kraft, G. R. Meehan, S. S. Murray, M. V. Zombeck, G. W. Fraser, J. F. Pearson, J. E. Lees et al., "Performance and calibration of the AXAF high-resolution camera I: Imaging readout," Proc. SPIE **3114**, 26–52 (1997).
- ²¹S. K. Lee, F. Cudry, Y. F. Lin, S. Lingenfelter, A. H. Winney, L. Fan, and W. Li, "Coincidence ion imaging with a fast frame camera," Rev. Sci. Instrum. **85**, 123303 (2014).
- ²² A. S. Tremsin and O. H. W. Siegmund, "Spatial distribution of electron cloud footprints from microchannel plates: Measurements and modeling," Rev. Sci. Instrum. **70**, 3282–3288 (1999).
- ²³ J.-J. Berthelier, J.-M. Illiano, D. Nevejans, E. Neefs, E. Arijs, and N. Schoon, "High resolution focal plane detector for a space-borne magnetic mass spectrometer," Int. J. Mass Spectrom. **215**, 89–100 (2002).
- ²⁴J. H. Chappell and S. S. Murray, "Position Modelin!Oor the AXAF high resolution camera (HRC)," Proc. SPIE 1159, 460–475 (1989).

- L. Krause, K. J. Schafer, and K. C. Kulander, "High-order harmonic generation from atoms and ions in the high intensity regime," Phys. Rev. Lett. 68, 3535 (1992).
 A. Zhao, M. van Beuzekom, B. Bouwens, D. Byelov, I. Chakaberia, C. Cheng, E. Maddox, A. Nomerotski, P. Svihra, J. Visser, V. Vrba, and T. Weinacht, "Coincidence velocity map imaging using Tpx3Cam, a time stamping optical camera with 1.5 ns timing resolution," Rev. Sci. Instrum. 88, 113104 (2017).
- ²⁷A. Nomerotski, "Imaging and time stamping of photons with nanosecond resolution in Timepix based optical cameras," Nucl. Instrum. Methods Phys. Res., Sect. A **937**, 26–30 (2019).
- ²⁸R. Meier and P. Eberhardt, "Velocity and ion species dependence of the gain of microchannel plates," Int. J. Mass Spectrom. Ion Processes **123**, 19–27 (1993).
- ²⁹ A. Mathew, G. B. Eijkel, I. G. M. Anthony, S. R. Ellis, and R. M. A. Heeren, "Characterization of microchannel plate detector response for the detection of native multiply charged high mass single ions in orthogonal-time-of-flight mass spectrometry using a Timepix detector," J. Mass Spectrom. **57**, e4820 (2022).
- ³⁰ X. Llopart, R. Ballabriga, M. Campbell, L. Tlustos, and W. Wong, "Timepix, a 65k programmable pixel readout chip for arrival time, energy and/or pho-ton counting measurements," Nucl. Instrum. Methods Phys. Res., Sect. A **581**, 485–494 (2007).
- ³¹C. Cheng, G. Moğol, T. Weinacht, A. Nomerotski, and C. Trallero-Herrero, "3D velocity map imaging of electrons with TPX3CAM," Rev. Sci. Instrum. **93**, 013003 (2022).
- ³²B. R. Sandel, A. L. Broadfoot, and D. E. Shemansky, "Microchannel plate life tests," Appl. Opt. **16**, 1435–1437 (1977).
- ³³S. Matsuura, S. Umebayashi, C. Okuyama, and K. Oba, "Characteristics of the newly developed MCP and its assembly," IEEE Trans. Nucl. Sci. **32**, 350–354 (1985).
- ³⁴D. T. Hall, "Ultraviolet resonance radiation and the structure of the heliosphere," Ph.D. thesis, The University of Arizona, 1992.
- ³⁵O. H. W. Siegmund, "Preconditioning of microchannel plate stacks," Proc. SPIE **1072**, 111–118 (1989).